

## Microstructure-based prediction of the elastic behaviour of hydrating cement pastes

Mazaheripour, Hadi; Faria, Rui; Ye, Guang; Schlangen, Erik; Granja, José; Azenha, Miguel

**DOI**

[10.3390/app8030442](https://doi.org/10.3390/app8030442)

**Publication date**

2018

**Document Version**

Final published version

**Published in**

Applied Sciences

**Citation (APA)**

Mazaheripour, H., Faria, R., Ye, G., Schlangen, E., Granja, J., & Azenha, M. (2018). Microstructure-based prediction of the elastic behaviour of hydrating cement pastes. *Applied Sciences*, 8(3), Article 442. <https://doi.org/10.3390/app8030442>

**Important note**

To cite this publication, please use the final published version (if applicable). Please check the document version above.

**Copyright**





Other than for strictly personal use, it is not permitted to download, forward or distribute the text or part of it, without the consent of the author(s) and/or copyright holder(s), unless the work is under an open content license such as Creative Commons.

**Takedown policy**

Please contact us and provide details if you believe this document breaches copyrights. We will remove access to the work immediately and investigate your claim.

Article

# Microstructure-Based Prediction of the Elastic Behaviour of Hydrating Cement Pastes

Hadi Mazaheripour <sup>1</sup> , Rui Faria <sup>1,\*</sup> , Guang Ye <sup>2</sup> , Erik Schlangen <sup>2</sup>, José Granja <sup>3</sup> and Miguel Azenha <sup>3</sup> 

<sup>1</sup> Civil Engineering Department, Faculty of Engineering, University of Porto (FEUP), 4200-465 Porto, Portugal; h.mazaheripour@gmail.com

<sup>2</sup> Microlab, Faculty of Civil Engineering & Geosciences, Delft University of Technology, Stevinweg 1, 2628 CN Delft, The Netherlands; g.ye@tudelft.nl (G.Y.); erik.schlangen@tudelft.nl (E.S.)

<sup>3</sup> ISE, Department of Civil Engineering, School of Engineering, University of Minho, 4800-058 Guimarães, Portugal; granja@civil.uminho.pt (J.G.); miguel.azenha@civil.uminho.pt (M.A.)

\* Correspondence: rfaria@fe.up.pt; Tel.: +351-225-081-950

Received: 7 February 2018; Accepted: 12 March 2018; Published: 15 March 2018

**Abstract:** The development of the elastic properties of a hardening cement paste results from the microstructural evolution due to cement hydration. The elastic behaviour of cement paste can be predicted by a combination of the hydration model and micromechanical analysis, which originates from a microstructural representative volume where the elastic behaviour of different hydrating cement products can be recognised. In this paper, the formation of the microstructural volume is simulated with the computational code HYMOSTRUC3D for cement hydration. The obtained microstructure is an input for a micromechanical modelling. A 3D regular lattice model is proposed to predict the elastic modulus of the microstructure, considering a water-to-cement ( $w/c$ ) ratio within the range [0.30–0.50]. In addition, the Finite Element Method (FEM) is used to compare and validate the results from the lattice model. Predictions from these two modelling approaches are then compared to the experimental results provided by the EMM-ARM (Elasticity Modulus Measurement through Ambient Response Method) testing technique, the latter allowing measurement of the elastic modulus of hydrating cement pastes. Finally, the above-referred numerical models are used to evaluate the influence of the following features: the particle size distribution of the cement grains, the microstructure discretisation refinement and the elastic modulus of the C-S-H cement hydration product.

**Keywords:** paste microstructure; HYMOSTRUC3D; lattice; FEM; elastic behaviour

## 1. Introduction

Most existing modelling practices for analysis of cement-based materials are based on continuum descriptions of their responses to external driving forces, namely stresses due to deformation gradients, heat fluxes due to temperature differences, diffusion due to concentration gradients, etc. These continuum approaches basically relate responses to the driving forces, considering the governing differential equations and the appropriate boundary conditions, which are usually solved with numerical methods such as the Finite Element Method (FEM). A fundamental aspect of these continuum approaches is the definition of constitutive laws that link the driving forces to the phenomenological responses which are generally based on accrued knowledge from macroscopic experiments. However, the problem complexity rises considerably when the approach aims to account for discontinuities, such as due to the pores network and micro-cracks. One practical limitation of using continuum approaches is the derivation of multi-variable phenomenological constitutive laws,

which usually demands unaffordable experimental programmes, particularly regarding coupled mechanisms, as it is the case of mechanical-transport modelling in porous media.

The basic idea of the present work is to derive the macroscopic constitutive laws of cement-based materials by modelling the physical processes at a small length scale, so that the constitutive laws may be looked as micromechanics-based, rather than being phenomenologically approximated. This aids scientists and engineers to bridge the gap between knowledge of microscopic mechanisms and the macroscopic responses, while they are still using continuum approaches with an acceptable accuracy for modelling complex phenomena. This modelling strategy is the genesis of continuum micromechanics approaches [1,2], in which a cement-based material is looked as a macro-homogeneous body, yet micro-heterogeneous, filling a Representative Elementary Volume (REV) with a prescribed characteristic length. Such REV includes homogeneous subdomains with the identification of known physical quantities that are called material phases [3]. Once their mechanical behaviour, shapes, and interactions are known at a small length scale, the overall homogenised mechanical behaviour of the material can be estimated.

One of the promising strategies for deriving the macroscopic constitutive law of a cement-based material is to model the cement paste microstructure using discretisation methods rather than continuum approaches, an example of the former being the lattice approach. A wide set of microstructural behaviour representations inside the cement paste can be constructed using lattices of space-filling polyhedra within the REV. Each polyhedron becomes a material phase in the microstructure, computationally represented as a lattice 'node' at the polyhedron centre, which is linked to the neighbouring 'nodes' using 'linear lattice beam elements'. The material mechanical behaviour at the macroscale is obtained by defining appropriate properties to the lattice elements and taking into account a homogenisation technique for upscaling. A fundamental requirement from the lattice model, to be highlighted for the present study, is that it has to reproduce the macroscopic elastic properties of the cement paste.

In addition, the cement paste microstructure can be appropriately reproduced only if the hydration of cement is well understood, and adequately accounted for in the numerical model. The total process of cement hydration is a complex chemical and physical set of phenomena, discussed worldwide by many researchers [4–6]. Several theoretical models have been developed to simulate the microstructure of the hardened cement paste, by considering the most dominant reactions that occur during hydration. Some of those well-known numerical hydration models are: (i) the Jennings and Johnson Model [7], (ii) the CEMHYD3D [8], (iii) the HYMOSTRUC3D [9,10] and (iv) the  $\mu\text{ic}$  [11]. The latest updated version of HYMOSTRUC3D was used in the present study to model the cement paste microstructure. HYMOSTRUC3D model uses a vector approach, with no theoretical limitation (apart from the required computational time) for considering the small size of the cement particles. These particles are assumed as spherical grains randomly distributed in the REV, which is typically considered as a cubic cell. The inward and outward growth of the spherical grains represents the hydration progress of the cement particles.

This paper is an extension of the work recently carried out by the authors [12], in which the cement paste microstructure is discretised with lattices of space-filling polyhedra. The main scope is devoted to modelling the elastic performance of cement pastes, accounting for the elastic moduli of the chemical phases and the interface elements at the microscale. The lattice model in [12], constructed based on cubic polyhedra [13,14], was not physically representative of the grains shape, the boundaries and the coordination with neighbouring grains. Furthermore, the preliminary model could not properly estimate the deformation of the microstructure due to the Poisson's effect, and thus a significant underestimation of the elastic modulus was obtained [12]. As an improvement, a lattice model based on truncated octahedrons is adopted in the present paper, showing a better performance to estimate the macroscopic elastic modulus of cement pastes, when compared to the previous model. The results obtained with the new lattice model are compared with the ones assuming a classical continuum approach but using a discretisation via the FEM, where 8-nodded solid hexahedral elements are

used. Predictions from lattice and FEM models are compared to experimental results obtained through the Elasticity Modulus Measurement through Ambient Response Method (EMM-ARM) testing technique, firstly developed in 2008 for concrete [15], and further enhanced to be used for cement pastes [16]. Finally, a numerical study was carried out towards evaluating the influence of some involved microstructural parameters on the predictions of the macroscopic elastic moduli of the cement pastes.

## 2. Material and Mixtures

A white cement, used as the primary binder by Muller et al. from 2012 to 2014 [17], is to be considered for the elasticity analysis in the present study. The batches of white cement were provided by Aalborg Portland. The mineral composition of this cement, as well as the cumulative Particle Size Distribution (PSD), are reproduced in Table 1 and Figure 1. The PSD can be fairly defined as a Rosin–Rammler function, i.e.,  $f(D) = 1 - e^{-bD^n}$ , where  $D$  is the diameter of the cement particle, and  $b$  and  $n$  are coefficients. By employing a curve fitting analysis, the values of 0.062 and 1.00 were calculated for  $b$  and  $n$ , respectively. The fitted curve is also plotted in Figure 1.

Table 1. Mineral composition of the white cement [12].

Cement Clinker Component	C3S	C2S	C3A	C4AF	Others	
Fraction (%)	66.89	20.59	3.62	1.03	7.87	
Density (g/cm <sup>3</sup> )	3.21	3.28	3.03	2.32	~3.0	Avg. 3.15

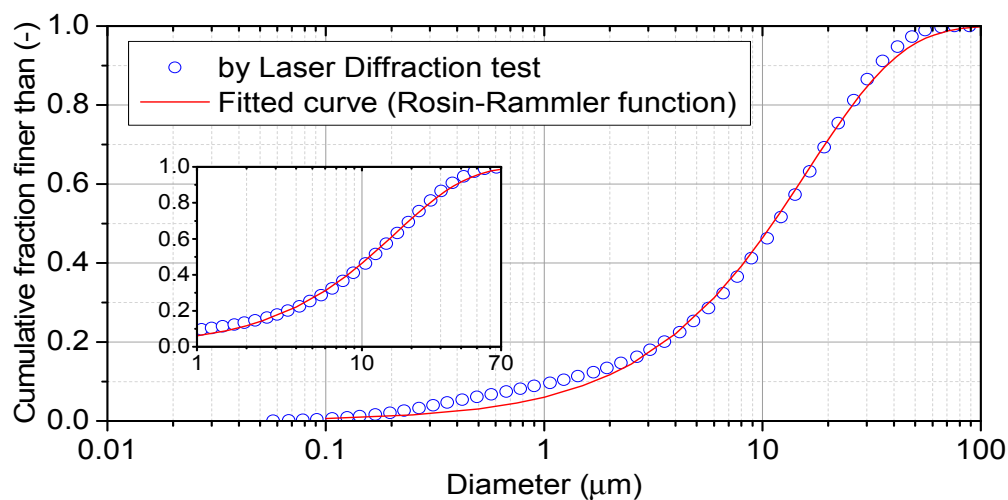


Figure 1. Particle Size Distribution (PSD) of the white cement and the fitted analytical curve.

Elastic properties of the individual components of cement clinker (e.g., Alite, Belite, etc.) can be experimentally measured by means of a nano-indentation testing technique at the microscopic scale, as reported by Velez et al. [18], or they can be calculated by force field atomistic methods, as recommended by Manzano et al. [19]. Young’s moduli of the major phases of Portland cement (i.e., C2S, C3S, C2A, and C4AF), reported by these authors, are provided in Table 2. An average value of these individual moduli is considered for the numerical simulations in the present study. The final elastic properties of the cement clinker are averaged by the weighting factors of the major phases as given in Table 1.

For preparing the cement paste, typically 80 g of anhydrous powder was mixed with water at the desired  $w/c$  mass ratios ( $w/c = 0.32, 0.40$  and  $0.48$ ). The mix was performed with the aid of plastic containers, using a paste mixer for 2 min at 1600 rpm [17]. Samples were then cured in a controlled temperature environment (at  $T = 20$  °C) in containers and used for parallel experiments.

**Table 2.** Elastic properties of cement clinker constituents.

Cement Clinker	Velez et al. (2001) [18]			Manzano et al. (2009) [19]			Present Study			Clinker		
	<i>E</i> (GPa)	<i>G</i> (GPa)	$\nu$ -	<i>E</i> (GPa)	<i>G</i> (GPa)	$\nu$ -	<i>E</i> (GPa)	<i>G</i> (GPa)	$\nu$ -	<i>E</i> (GPa)	<i>G</i> (GPa)	$\nu$ -
Alite (C <sub>3</sub> S)	135	51.9	0.3	138.9	54.5	0.28	137	53	0.30			
Belite (C <sub>2</sub> S)	130	50.0	0.3	137.9	53.1	0.3	134	52	0.30			
C <sub>3</sub> A	145	55.8	0.3	-	-	-	145	56	0.30	137	53	0.3
C <sub>4</sub> AF	125	48.1	0.3	-	-	-	125	48	0.30			

*E*: Elastic modulus; *G*: Shear modulus;  $\nu$ : Poisson’s ratio.

### 3. Microstructure of the Cement Paste

In the present study the latest version of HYMOSTRUC3D computer software [10], developed in the Materials & Environment Department at Delft University, is used for the construction of the cement paste microstructure during hydration. This simulation is implemented in a cubic REV volume of the cement paste where the cement particles are modelled as spheres randomly distributed. The initial number and diameter of the particles are built in accordance with the PSD—see Figure 1. The main cement hydration products are the Calcium-Silicate-Hydrate (C-S-H) and the Calcium Hydroxide (CH). C-S-H is formed as two layers of inner and outer products, which are the result of the inward and outward radial growing of the cement spheres, as shown in Figure 2a. Figure 2b presents the interaction between the cement particles during the hydration process in the REV. Examples of the simulated microstructure of the cement paste after 1 h and 156 h of hydration are depicted in Figure 3.

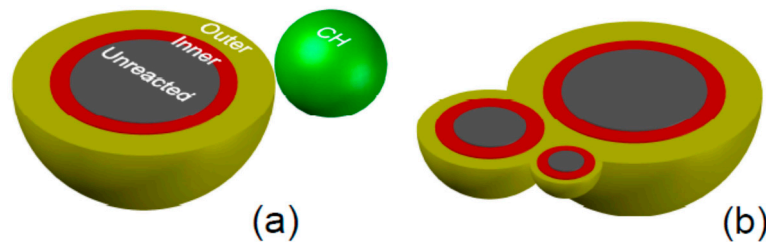


**Figure 2.** (a) Cement hydration products in HYMOSTRUC3D, (b) Overlapping of the product layers in particle contacts.

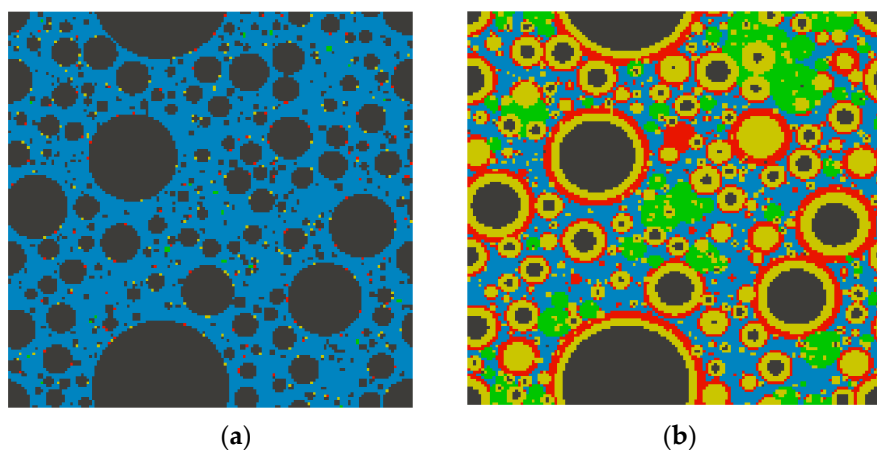


**Figure 3.** Microstructure formation of the cement paste in a 2D view: (a) after 1 h of hydration; (b) after 170 h of hydration (grey: unreacted cement grain; red: Inner C-S-H; yellow: Outer C-S-H; green: CH grain; blue: water or void).

The important parameters to be defined in HYMOSTRUC3D for modelling cement hydration are summarised in Table 3. For further details on fundamental aspects of the model parameters, the reader is addressed to the studies published by Van Breugel and by Guang Ye [10,20]. The hydration parameters shown in Table 3 were calibrated using the degree of hydration measured through isothermal calorimetry, performed on the same cement for different  $w/c$  ratios [17]. The experimental and numerical results are plotted and compared in Figure 4. By giving a relevant set of hydration parameters to the model, a good estimation is obtained regarding the degree of reaction for the three cement paste mixtures under study.

**Table 3.** Main model hydration parameters in HYMOSTRUC3D.

Model Hydration Parameters	$w/c = 0.32$	$w/c = 0.40$	$w/c = 0.48$
$k_0$ (reaction rate of cement particle)	0.035	0.055	0.04
$d_{tr}$ (transition thickness of cement particles)	2.0	2.0	2.0
$\beta_1$ (calibration parameters)	1.0	1.0	1.0
$\beta_2$ (calibration parameters)	1.0	1.0	1.0
Dimensions the REV cube	$100 \times 100 \times 100 \mu\text{m}^3$		
Reactant	C3S, C2S, C3A, C4AF, and gypsum		
Product phases	Inner layer C-S-H; Outer layer C-S-H; CH grain		
Minimum and maximum particle size	$1 \mu\text{m} - 70 \mu\text{m}$		
Temperature	$20^\circ\text{C}$		
PSD parameters: $b, n$	0.06, 1.0 (see Figure 1)		

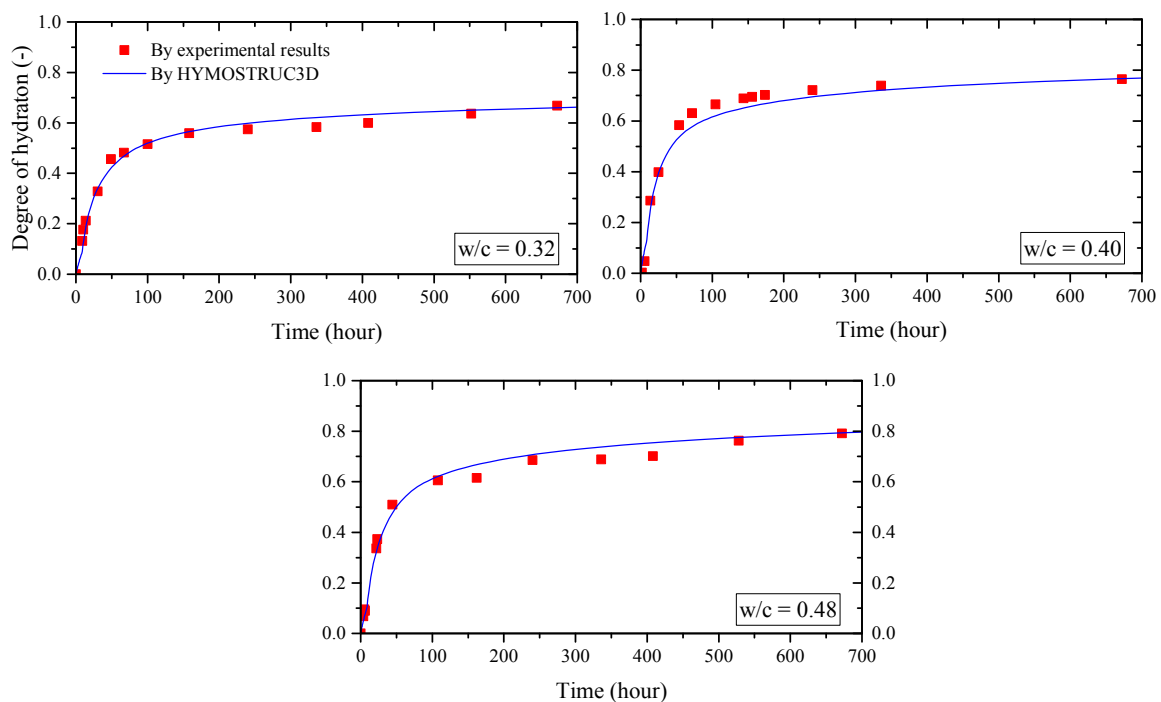


**Figure 4.** The degree of hydration predicted by HYMOSTRUC3D and measured by isothermal calorimetry.

#### 4. Mechanical Model

To assess the evolution of elasticity in the cement paste, the simulated microstructure—a REV with dimensions  $100 \times 100 \times 100 \mu\text{m}^3$ —is initially discretised into small  $1.0 \times 1.0 \times 1.0 \mu\text{m}^3$  cubic voxels. Two mechanical approaches, described in the following sections, are adopted to predict numerically the effective elastic modulus of the simulated REV microstructure of the cement paste: (i) the lattice and (ii) the FEM models.

#### 4.1. Lattice Model

Lattice models have been used to simulate the fracture mechanism and transport properties of cement-based [13,21] and other quasi-brittle materials, especially when highly heterogeneous. The previous lattice model adopted by the authors in [12] significantly underestimated the experimental results, and the results obtained from the FEM model. This shortage was mainly because the simple regular assembly adopted in the lattice construction could not simulate the Poisson's effect that naturally occurs in solid materials, which is well captured by using the FEM. In fact, the lattice model can represent an isotropic homogeneous linear elastic material when the Poisson's ratio equals zero, which is a direct result for a cubic lattice [22]. As an alternative, irregular lattices have been proposed in the literature, such as those constructed from Delaunay triangulations by assuming 3D volumes [23–26]. However, they are not recommended for the aim of material modelling in which the establishment of a link between the macroscopic elastic properties and the local elastic behaviour of the assembly elements is purposed. To overcome such shortage, a 3D regular lattice model based on a regular cellular assembly of truncated octahedrons [27] is adopted in the present study, and briefly described in the following subsections.

##### 4.1.1. Lattice Construction

The adopted 3D lattice is constructed using individual unit cells as shown in Figure 5a. It includes two types of nodes (middle and corner nodes) and beams. The corner nodes are connected by regular lattice beams, named as Beam 1, whereas the middle and corner nodes are linked with diagonal beams, named as Beam 2 (see Figure 5a). Therefore, each unit cell includes eight diagonal and 10 regular lattice beams. For constructing the 3D lattice model, the unit cell should be located in the discretised microstructure obtained from HYMOSTRUC3D, in the way depicted in Figure 5b. By adopting the same dimension for the lattice unit cell as defined for each voxel (i.e.,  $1.0\ \mu\text{m}$ ), the corner nodes should be precisely located in the centre of the eight neighbouring voxels (see dotted cubes in Figure 5b), and the middle node is placed at the vertices of the cubic voxel (see darker node in Figure 5b). By filling all the voxels with the lattice unit cell, the complete 3D lattice model is constructed. In Figure 6a, it is shown an example of the 3D regular lattice constructed by using the obtained microstructure after about 7 days of hydration. Different colours represent different material phases in the model, as defined in the figure's caption.

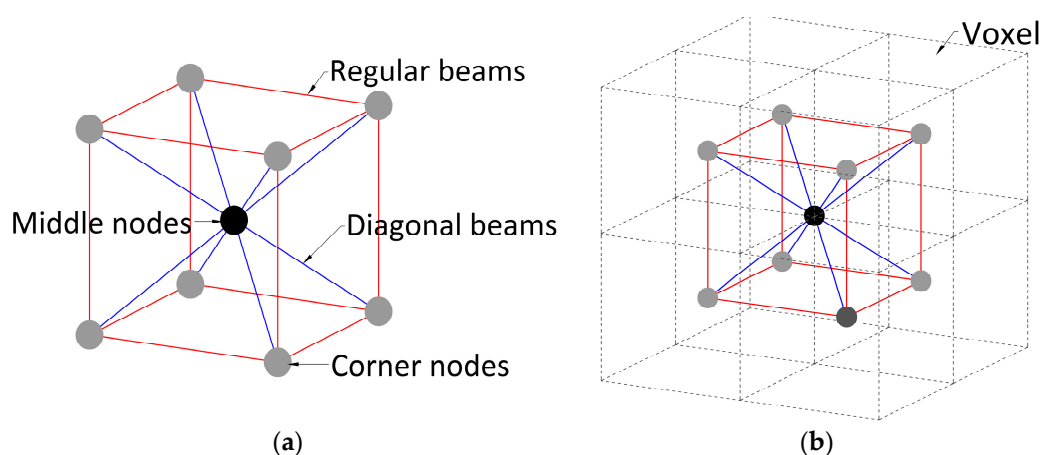


**Figure 5.** (a) Construction of the lattice unit cell based on truncated octahedral; (b) positioning of the lattice unit cell on the discretised Representative Elementary Volume (REV) voxels.

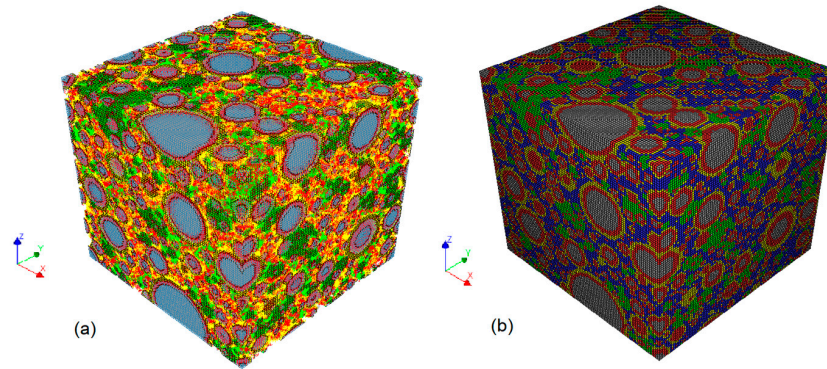


**Figure 6.** (a) 3D regular lattice model, (b) FE model—grey: unreacted cement, red: C-S-H inner, yellow: C-S-H outer, green: CH, black: all interface beams, blue: pore phases.

#### 4.1.2. Boundary Conditions and Effective Elastic Modulus

The constructed lattice model is imported to DIANA FEA computer software (released version 10.1), which is the numerical solver chosen in the present study. The configuration of a uniaxial tensile test setup is considered for evaluation of elastic modulus in DIANA FEA. Therefore, the uniaxial test is configured for the REV microstructure by fixing all the nodes on the bottom surface of the specimen (plane  $Z = 0$ ), and imposing a uniform surface displacement on the top surface ( $Z = n \cdot l$ , where  $n$  is the number of voxels along the  $Z$  direction). Young’s modulus of the different cement paste phases is assumed to equal in both compression and tension. Thus the loading sign has no relevance for the present simulations. The lattice model is solved in tension by imposing a prescribed displacement of  $10^{-4} \mu\text{m}$  to the top surface nodes (plane  $Z = n \cdot l$ ). The effective elastic modulus is derived from the following equation:

$$E_{eff} = \frac{R \cdot L_{eff}}{A_{eff} \cdot \Delta_{long}} \quad (1)$$

where  $R$  is the total reaction force in the supports at  $Z = 0$  on a direct tensile load test and  $A_{eff}$  is the effective area (equal to the area of each external surface of the cubic REV).  $L_{eff}$  is the effective length (equal to the distance between the two opposite loaded REV faces) and  $\Delta_{long}$  is the total longitudinal displacement in REV ( $10^{-4} \mu\text{m}$ ). It should be noted that the differences between the results when loading along direction  $Z$  or along directions  $X$  or  $Y$  were negligible (less than 1%), meaning that the effective elastic modulus is not influenced by the loading direction in the REV.

The Poisson’s ratio is evaluated based on the transverse contraction strain  $\epsilon_{trans}$  and the longitudinal strain  $\epsilon_{long}$ :

$$\nu_t \cong -\frac{\epsilon_{trans}}{\epsilon_{long}} \cong -\frac{\Delta_{trans}}{\Delta_{long}} \quad (2)$$

where the transverse displacement  $\Delta_{trans}$  is calculated by drawing the REV deformed configuration, and taking a linear regression along the faces parallel to the direction of loading, as suggested in [3,26].

#### 4.1.3. Beam Elements

The Class-I FE beam available in DIANA FEA is assigned for both lattice Beams 1 and 2. Class-I FE beam is a two-nodded straight element that has 12 degrees of freedom (D.O.F): three displacements and three rotations at each extremity [28]. The Class-I FE is based on the Timoshenko theory [29,30], which accounts for the shear deformation.

#### 4.1.4. Definition of Beam Properties

Mechanical properties of Beam 1 are defined by the location of the two nodes at the extremities. If the nodes are positioned in the same phase (two voxels with the same material phase), Beam 1 has



the mechanical properties of the respective phase; if not, an interface beam is considered between the two connected phases. Definition of the elastic properties of the interface beam should be based on relevant material tests. However, due to lacking data from such experiments, Young’s modulus of the interface beam can be calculated based on the serial/parallel rule of mixtures for composite materials, as pursued by Qian et al. [14]. Based on this theory, an interface element is considered as a two-phase material with a lower-bound Young’s modulus of:

$$\frac{1}{E_l^I} = \frac{v_A}{E_l^A} + \frac{(1 - v_A)}{E_l^B} \tag{3}$$

where  $E_l^I$ ,  $E_l^A$  and  $E_l^B$  are, respectively, the local Young’s moduli of the interface and phase A and phase B beams.  $v_A$  is the volumetric fraction of phase A, taken as 0.5, assuming an equal contribution of phases A and B.

Alternatively, the effective Young’s modulus of the interface material can be calculated using the classical Hashin–Shtrikman bounds method [31]. According to this method, the local bulk modulus of a two-phase composite material can be described by a matrix of phase A (a material with a lower bulk modulus), within which spherical inclusions of phase B (a material with higher bulk modulus) are distributed in a particular way [31]. This is mathematically expressed as follows:

$$K_l^I = K_l^A + \frac{(1 - v_A)}{\frac{1}{K_l^B - K_l^A} + \frac{3v_A}{3K_l^A + 4G_l^A}} \quad (K_l^B > K_l^A) \tag{4}$$

where  $K_l^I$ ,  $K_l^A$  and  $K_l^B$  are the local bulk moduli of the interface and phase A and B beams, respectively.  $G_l^A$  is the local shear modulus of material phase A. As the independent elastic properties of a material are Young’s modulus  $E_l$  and the Poisson’s ratio  $\nu_l$ , the local bulk and shear moduli for each phase are:

$$K_l = \frac{E_l}{3(1 - 2\nu_l)} \tag{5}$$

$$G_l = \frac{E_l}{2(1 + \nu_l)} \tag{6}$$

The difference between using Equations (3) and(4) is shown in Figure 7 by plotting the dimensionless ratio  $E_l^I/E_l^A$  versus  $E_l^B/E_l^A$ . By increasing the difference between Young’s modulus of material phases A and B, both methods give higher values for the interface Young’s modulus, being the value from Hashin–Shtrikman theory always higher than that from the serial/parallel rule. In Figure 7, the vertical dotted lines indicate the theoretical range of  $E_l^B/E_l^A$  for the cement paste microstructure of present study. Both theories are used for calculation of the effective Young’s modulus of the interface elements, and the respective results will be discussed in Section 6.1.

The local tensile strength of the interface beam is defined as the minimum value between the tensile strength of phases A and B (i.e.,  $\min\{f_{Tl}^A, f_{Tl}^B\}$ ). Although it has been previously reported that the interface strength may not be the minimum of the corresponding phases [25], the local tensile strength is not relevant for the present study, as fracture behaviour is not addressed here.

On the other hand, the mechanical properties of Beam 2 (diagonal) are defined only based on the properties of the middle node. This means that none of the Beam 2 counted as an interface beam.

The intrinsic elastic properties of the individual phases of the cement paste are defined based on the values reported in the literature. There are ranges of values for the elastic properties of C-S-H inner and outer products, depending on their porosity. In the present study, the average values reported in Table 4 are adopted, in accordance with the recent study carried out by Sekkal et al. [32]. Note that the elastic properties of the unreacted cement were previously given in Table 2.

**Table 4.** The elastic properties of hydration products adopted in the modelling.

Hydration Product	Elastic Modulus (Average Value) (GPa)	Poisson's Ratio
C-S-H Inner (high-dense)	26–32 (29)	0.25
C-S-H Outer (low-dense)	13–26 (19.5)	0.25
CH	35	0.30

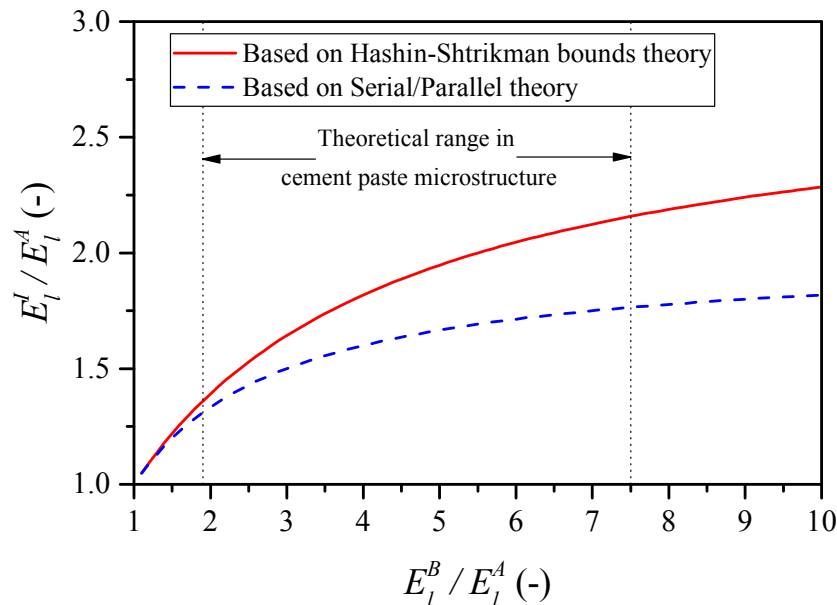


**Figure 7.** Effective Young’s modulus of an interface element calculated with two different methods: the serial/parallel and the Hashin–Shtrikman classical bounds theory

#### 4.1.5. Definition of Beam Geometry

Both lattice Beams 1 and 2 are assumed as cylindrical bars, with a constant circular cross-section. Lengths  $l_1$  for Beam 1 and  $l_2$  for Beam 2 can be directly calculated from the coordinates at their nodal extremities. In the proposed regular model, these values are constant and given by:

$$l_1 = l, l_2 = \left(\sqrt{3}/2\right)l \tag{7}$$

where  $l$  is the length of the voxels, adopted as  $1.0 \mu\text{m}$  in this study.

However, calculation of diameters  $d_1$  for Beam 1 and  $d_2$  for Beam 2 is not straightforward. Let us assume an isotropic and homogenous cubic REV of  $20 \times 20 \times 20 \mu\text{m}^3$ , discretised with voxels of  $1 \times 1 \times 1 \mu\text{m}^3$ . Each voxel represents a single material phase, with a local Young’s modulus  $E_l$ . A 3D lattice model constructed with this REV-based unit cell is reproduced in Figure 5a, where  $L_{eff} = 20$  and  $l = 1.0$ . The uniaxial tensile boundary conditions described in Section 4.1.2 are assigned to this lattice model, as shown in Figure 8a. For  $d_1/l_1$  and  $d_2/l_2$  ranging from 0.2 to 2.0, the results of the lattice model in terms of  $E_{eff}/E_l$  are reproduced in Figure 9a as a surface. An example of the deformation field obtained from such direct tensile test is illustrated in Figure 8a. By increasing both  $d_1/l_1$  and  $d_2/l_2$ , the value of  $E_{eff}/E_l$  increases significantly. Since the model is homogenous (a single phase REV is considered), theoretically the following condition has to be satisfied:

$$E_{eff} = E_l \tag{8}$$

meaning that the calculated effective Young’s modulus must be equal to Young’s modulus of the individual phase. If the  $E_{eff}/E_l$  surface intersects the surface  $E_{eff}/E_l = 1$ , the corresponding values

for  $d_1/l_1$  and  $d_2/l_2$  meets the condition in Equation (8). Since the REV is elastic and isotropic, the best set of values for  $d_1/l_1$  and  $d_2/l_2$  can be selected based on the most representative lateral deformation of the lattice model due to the Poisson's effect, that is:

$$v_t = v_s \tag{9}$$

being

$$v_s = \frac{E_{eff}}{2G_{eff}} - 1 \tag{10}$$

where  $G_{eff}$  is the effective shear modulus that can be obtained by modelling a direct shear test as shown in Figure 8b. A prescribed shear deformation along direction Y is applied to the nodes at the top surface of REV (plane  $Z = n \cdot l$ ), while the nodes at the bottom surface (plane  $Z = 0$ ) are fixed in the Z and Y directions. The obtained shear deformation field is illustrated in Figure 8b. The value of  $G_{eff}$  is calculated similarly as for  $E_{eff}$  using Equation (1), where  $\Delta_{long}$  is replaced by the transversal deformation along direction Y for the nodes at  $Z = n \cdot l$ .

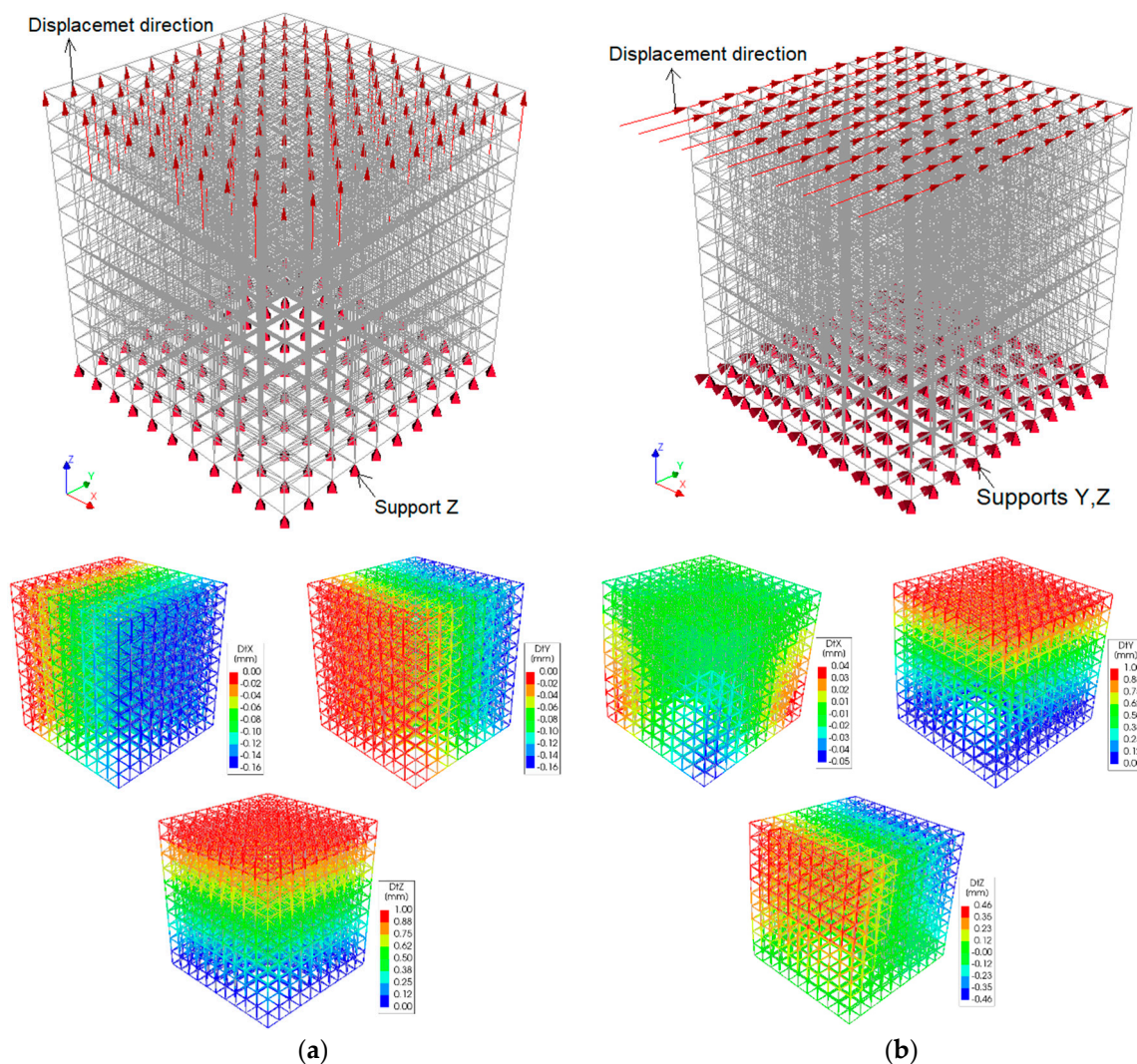


**Figure 8.** The configuration of a homogeneous lattice model of a  $20 \times 20 \times 20 \mu\text{m}^3$  REV and deformation fields: (a) direct tensile model; (b) direct shear model (DtX, DtY, and DtZ are, respectively, deformation in X, Y and Z directions).

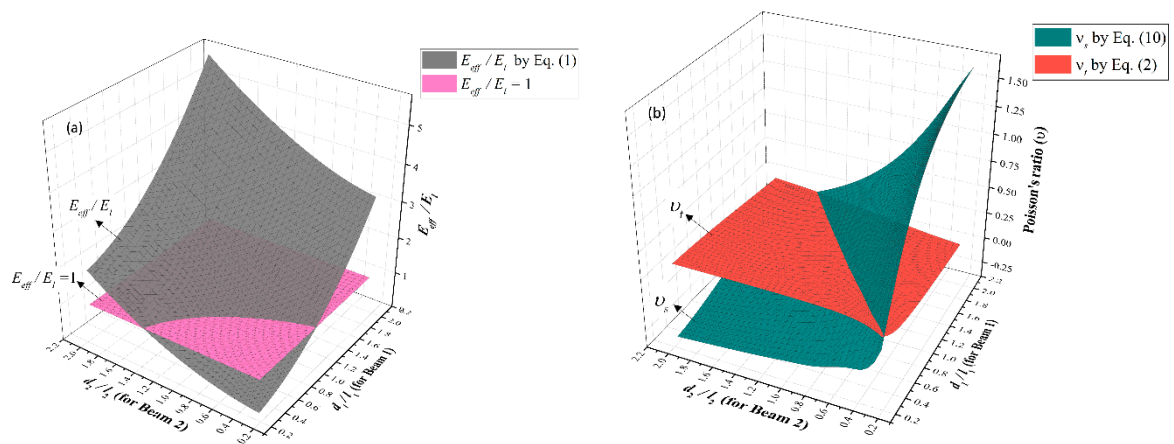


**Figure 9.** Homogeneous and isotropic lattice model for a  $20 \times 20 \times 20 \mu\text{m}^3$  REV for variations of  $d_1/l$  and  $d_2/l$  regarding (a)  $E_{eff}/E_l$ ; (b) Poisson's ratio.

Predictions for  $v_t$  obtained with Equation (2), and for  $v_s$  using Equation (10) (with  $d_1/l_1$  and  $d_2/l_2$  ranging from 0.2 to 2.0), are plotted in Figure 9b. As shown, the intersection of the two obtained surfaces for  $v_t$  and  $v_s$  corresponds to values of  $d_1/l_1$  and  $d_2/l_2$ , where  $v_t = v_s$ . This intersectional curve for  $v_t = v_s$ , and the one in Figure 9a for  $E_{eff}/E_l = 1$ , are separately plotted in Figure 10. As it can be seen, the intersection of the two curves leads to a single definition of  $d_1/l_1$  and  $d_2/l_2$ , with allowing fulfilment of elastic isotropy and homogeneity assumptions. According to this calibration strategy,  $d_1/l_1 = 0.895$  and  $d_2/l_2 = 0.748$  are the geometrical data to be adopted for Beams 1 and 2 in the heterogeneous lattice models, where each voxel phase is considered a homogeneous elastic isotropic material.

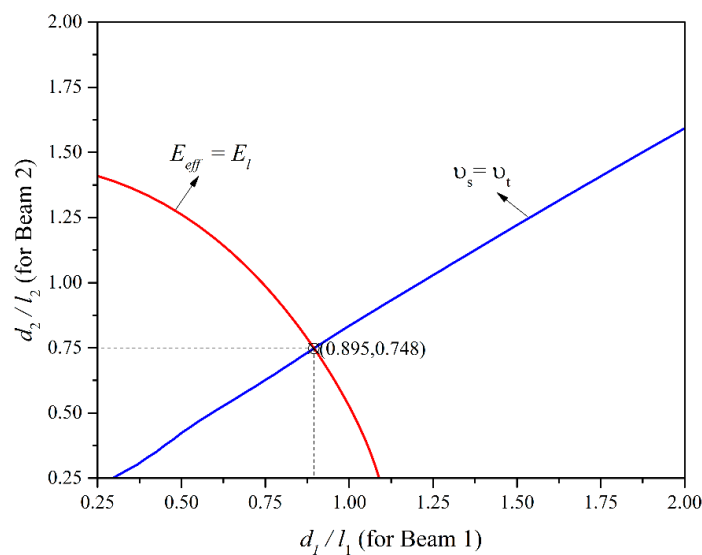


**Figure 10.** Calibrated geometrical values for  $d_1/l$  and  $d_2/l$  are assigned to, respectively, Beams 1 and 2 in the proposed lattice model.

#### 4.2. FEM Model

Definition of the FE model is straightforward as each cubic voxel from the microstructure is easily converted to an 8-nodded solid. The FE model is also solved in DIANA FEA, employing an 8-nodded isoparametric solid brick element with a  $2 \times 2 \times 2$  Gauss integration scheme (further details can be found in [28]). Each solid element represents one hydrating cement phase (e.g., inner product,

CH grain, etc.), while no finite element is created for the pore voxels. The FEM model does not have any interface beam. The elastic properties of each FE are defined by the ones of the corresponding solid phase, as previously documented in Tables 2 and 4. Boundary conditions in the FEM model are similar to the ones in the lattice model, with all the nodes located on the bottom surface assumed as fixed, while a prescribed displacement is imposed on the top surface nodes. The constructed FEM model from the microstructure obtained from HYMOSTRUC3D after about 7 days of hydration is illustrated in Figure 6b.

## 5. EMM-ARM Testing Method

The Elasticity Modulus Measurement through Ambient Response Method (EMM-ARM) is a testing technique that can be used for the continuous measurement of the E-modulus of a given cement paste during hydration. In this test, Young's modulus of the paste can be continuously measured since the onset of casting. The technique is under development since 2008 and in its version targeted for testing cement paste. It is based on the identification of the resonant frequency of a cantilever, constituted by a cylindrical plastic mould filled with the paste to be characterised. The experimental results obtained from the EMM-ARM for white cement paste with the  $w/c$  ratios of 0.32, 0.40 and 0.48 are used next for validation of the microstructure-based mechanical models described in the previous section. The testing configuration of EMM-ARM is schematically illustrated in Figure 11. More details about the test and results can be found in [16].

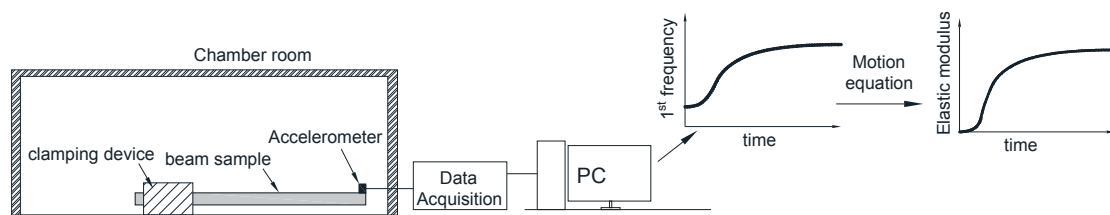


**Figure 11.** Experimental setup for the Elasticity Modulus Measurement through Ambient Response Method (EMM-ARM) testing of cement paste and data processing.

## 6. Results and Discussion

### 6.1. Lattice vs. FEM Results

The Young's modulus and the Poisson's ratio predicted by the lattice and FEM models at different hydration ages for the white cement paste with  $w/c = 0.40$ , and some computational details about the numerical models, are provided in Table 5. The number of nodes and elements in the lattice model is much higher than the FEM model. Therefore, the computational time that is required to solve the lattice model is significantly higher than the FEM model. However, as it was addressed earlier, the advantages of using lattice models become visible when solving a fracture behaviour, transport problems, or using combined problems in cement paste is intended.

Performances of the lattice and FEM models are illustrated in Figure 12a, by comparing their predictions for the effective Young's modulus of the cement pastes. Results from the lattice model fit nicely to those obtained by the FEM, with an error less than 2%. The error becomes less than 0.62% when the Hashin–Shtrikman theory is used to define Young's modulus for the interface elements. Young's modulus of the interface elements has no significant effect on the effective elastic properties because only 8% of all lattice elements are interface elements (see Table 5). Figure 12b compares the two numerical approaches as far as the Poisson's ratio of the cement pastes is concerned, the conclusion is that the lattice model nicely captures the Poisson's ratio from the FEM model. Therefore, the improved lattice model for predicting Young's modulus and the Poisson's ratio of the cement pastes performs much better than the lattice model adopted in [12].

**Table 5.** Computational details for the lattice and Finite Element Method (FEM) models for  $w/c = 0.40$ .

Hydration Time (Hours)	Model	Number of Element	Number of Nodes	Number of Interfaces	Interface Percentage (%)	Solving Time * (sec)	Young's Modulus (GPa)	Poisson's Ratio (-)
5	Lattice	5,199,531	1,366,992	222,459	4.28	2641	3.60	0.248
	FE	515,200	897,518	-	0.0	242	3.62	0.237
15	Lattice	6,042,059	1,486,326	431,944	7.15	2932	6.32	0.252
	FE	593,551	942,238	-	0.0	242	6.32	0.239
28	Lattice	6,688,144	1,564,456	543,773	8.13	3145	9.56	0.253
	FE	651,815	964,251	-	0.0	263	9.53	0.241
50	Lattice	7,278,024	1,630,933	578,575	7.95	4086	12.31	0.255
	FE	704,181	979,932	-	0.0	271	12.34	0.239
84	Lattice	7,557,111	1,660,055	572,667	7.58	4592	13.84	0.257
	FE	728,502	985,321	-	0.0	274	13.86	0.241
111	Lattice	7,725,450	1,677,884	574,797	7.44	5123	14.72	0.261
	FE	743,217	988,786	-	0.0	281	14.68	0.243
156	Lattice	7,904,593	1,696,642	577,694	7.31	5637	15.32	0.263
	FE	758,822	992,332	-	0.0	296	15.32	0.246

\* As reported by DIANA FEA for the whole process including solving and output writing, and obtained using a desktop computer.

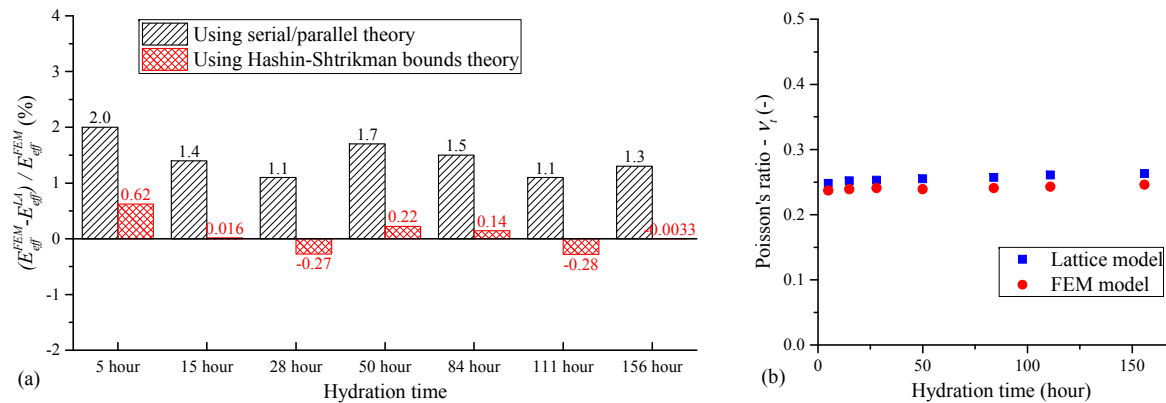


**Figure 12.** Elastic results of lattice and FEM models regarding (a) Young's modulus; (b) Poisson's ratio.

## 6.2. Experimental vs. Numerical Results

The effective Young's modulus predicted by the lattice and FEM models are compared in Figure 13 with the experimental measurements from the EMM-ARM testing technique for the cement pastes with  $w/c$  ratios of 0.32, 0.40 and 0.48, at different hydration ages. For the  $w/c$  ratios of 0.32 and 0.40, there is an acceptable predictive performance from the two numerical models, though the results at very early ages ( $\sim 5$  h) are highly overestimated. At very early ages, the cement paste changes from a liquid to a solid phase, being rather difficult and complex to capture such solidification transition with the available mechanical models. The packing density of C-S-H is low at very early ages, so considering constant values for the elastic moduli of C-S-H phases during this hydration stage may be unrealistic. In Section 6.3.3, the dependency of the effective elastic modulus of the cement paste on Young's modulus of C-S-H will be discussed. On the other hand, the ratio of the volume of connected solid phases to the total volume of the solid phase (the so-called "solid percolation threshold" [33]) plays an important role to estimate the elastic modulus of the cement paste correctly. The percolation threshold is influenced by the resolution of the mechanical model as concluded by Ye et al. [34]. In Section 6.3.2, the influence of voxel size on the predictions of the effective elastic modulus at early ages of cement pastes will be analysed. Moreover, Young's modulus may be influenced by cohesion between solid particles, and not only by their contact as it was reported by Torrenti and Benboudjema [35]. This effect, which was named as "mechanical percolation threshold" [35], was not included in the mechanical FEM model. In the case of the lattice model, an averaged property of two connected solid phases was defined for the interface beams, which may not represent the real cohesion formed between the solid particles.

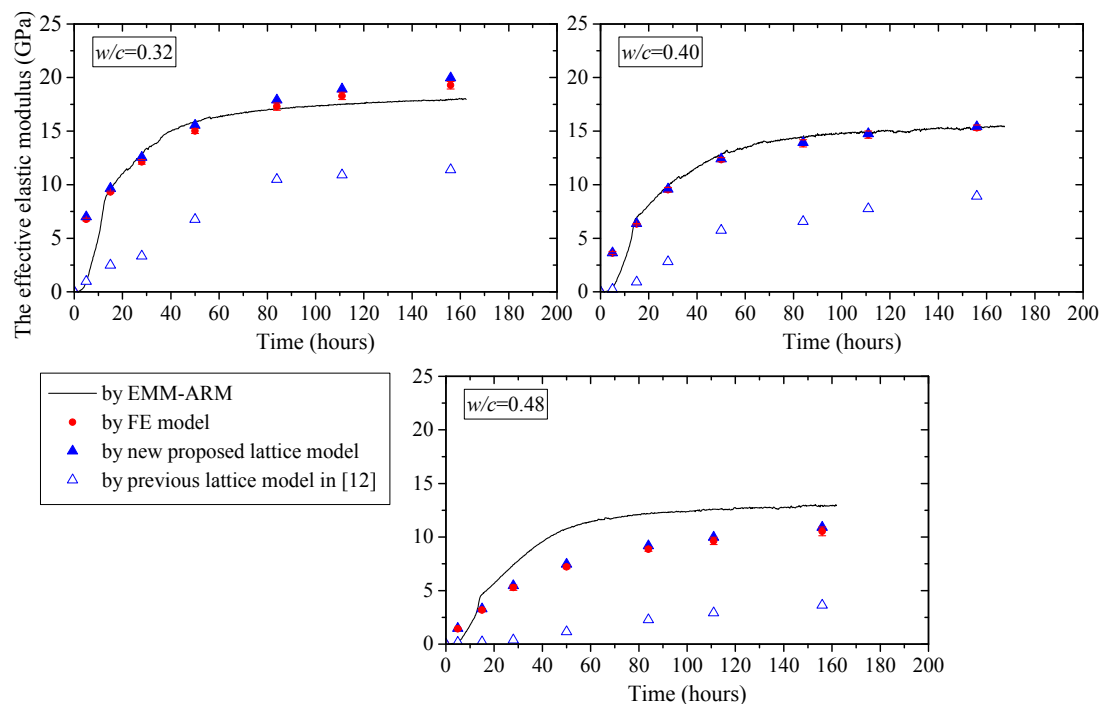


**Figure 13.** Young's modulus of the cement paste: experimental vs. numerical results.

The predictive performance of both numerical models decreases for the  $w/c = 0.48$ , leading to an underestimation of the experimental results (Figure 13). The performance of the numerical models depends on many involved parameters. Among them, the accuracy of HYMOSTRUC3D to predict the pore size distribution is possibly the most important one, since it has a direct link to the morphology of the microstructure, and consequently to the solid phase connectivity in the simulated

microstructure [36]. By increasing the  $w/c$ , this effect is more significant since the number of capillary porosity increases. In the recent study by Gao et al. [37], a good agreement was reported between the pore size distribution (both capillary and gel pores) predicted by HYMOSTRUC3D and those obtained by SEM and MIP testing methods, for a Portland cement paste at ages ranging from 1 to 28 days. However, the porosity provided by HYMOSTRUC3D contradicts the results obtained from the  $^1\text{H-NMR}$  testing technique [17] for the materials under testing. It is also criticised that  $^1\text{H-NMR}$  does not measure all the volume of capillary pores since only pores filled by capillary water are measured for a sealed cement paste sample. Further analysis is thus still required for validation of mechanical properties on the same paste evaluated at different  $w/c$  values, and tested by SEM, MIP and possibly  $^1\text{H-NMR}$ . Regardless of the deficiency that was observed for the cement paste with  $w/c = 0.48$ , the overall predictive performance of both the lattice and FEM models can be acceptable.

To evaluate the influence of several parameters on the effective Young's modulus of cement pastes, a parametric study is carried out in the following sections. For this purpose, the cement paste with  $w/c = 0.40$  is considered by using the FEM model as for evaluating the elastic behaviour of the microstructure this model is computationally more economical, and besides no significant differences were observed on the performances of the lattice and FEM models (see Figure 12).

### 6.3. Parametric Study

#### 6.3.1. Influence of PSD

Two different PSD curves were considered by changing the parameters  $b$  and  $n$ , as plotted in Figure 14a. Using the first PSD curve (red line, with  $b = 1.1$ ,  $n = 0.07$ ) gives a higher number of cement particles in the REV, whilst using the second curve (blue line, with  $b = 0.95$ ,  $n = 0.05$ ) gives less. This difference in the number of cement particles obviously leads to two different Blaine indexes for the cement, which are indicated in Figure 14a. Simulations with the FEM model were carried out adopting these two curves, and the calculated effective elastic moduli are plotted in Figure 14b. There is a significant influence on the effective Young's modulus of the REV when the number of particles is changed. In fact, the change in the PSD curve influences the pore distribution size formed in the REV. A finer PSD curve leads to a finer pore network, and consequently to higher Young's modulus. Thus, errors in PSD measurements, or any change in the PSD during mixing with water or along the casting process, have a significant influence on the cement paste elastic properties.

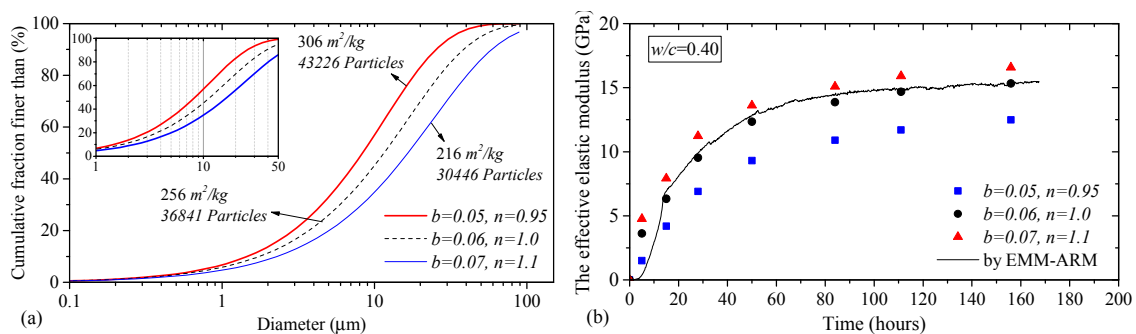


**Figure 14.** (a) Three adopted PSD curves in the hydration model by HYMOSTRUC3D; (b) Young's moduli obtained for the three different PSD curves.

#### 6.3.2. Influence of Voxel Size

Most of the hydration models, including the HYMOSTRUC3D, are based on the vector approach [11] which assumes cement grains as spheres, being able to grow inwards and outwards, or to nuclei inside the REV. The precision of the numerical model is dependent on the resolution of voxels that discretises these spheres. The results of different voxel sizes implemented for discretisation



of REV are plotted in Figure 15 for  $w/c = 0.40$ . As shown in this figure, by decreasing the voxel size the effective Young's modulus of the cement paste also decreases. However, there is no significant change when the voxel size is considered less than about 70% of the minimum particle size ( $1.0 \mu\text{m}$ )—see the results for the voxel size of  $0.57 \times 0.57 \times 0.57 \mu\text{m}^3$ . In fact, the voxel size of  $0.67 \times 0.67 \times 0.67 \mu\text{m}^3$  can be an optimised voxel size for discretisation of the REV. This can be explained by the fact that the artificial solid phase connection becomes a minimum when the voxel size decreases. When the artificial solid phase connection decreases, it reduces the total solid part connectivity in REV, leading to a decrease of the effective Young's modulus. This resolution is important to capture properly the effect due to the solid percolation threshold of the cement paste at very early ages. As shown in Figure 15, at the age of  $\sim 5$  h, and decreasing the voxel size from  $1.25 \mu\text{m}$  to  $0.57 \mu\text{m}$ , the accuracy of the model to estimate the experimental value increases.

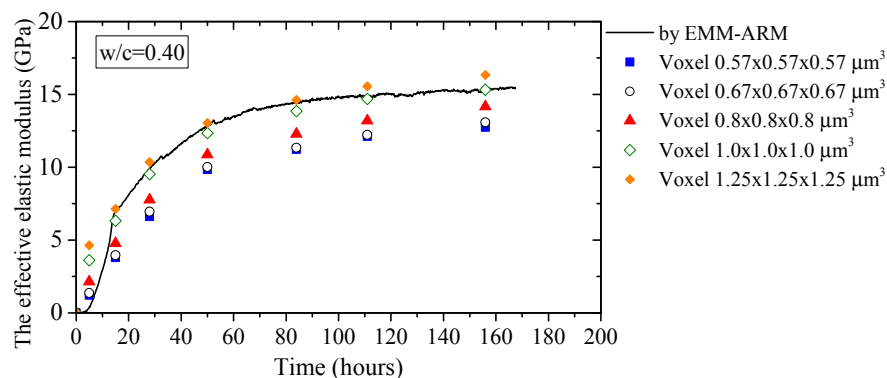


**Figure 15.** Influence of voxel resolution on the effective elastic Young's modulus of REV.

The influence of voxel resolution on the effective Young's modulus can be considered as a modelling weakness as far as predicting mechanical properties of the microstructure is concerned. The choice of the voxel resolution is directly limited by the available computational power, and sometimes by algorithmic problems (such as convergence).

### 6.3.3. Influence of Elastic Properties of C-S-H

Despite the Portlandite CH product, the crystal structure of C-S-H in the cement paste is not yet fully known, and there is still ongoing debate over its nanostructure. In the literature, C-S-H is typically divided into two different phases, with different packing densities, and consequently with two different Young's moduli. A wide range of measured values for the corresponding elastic properties is reported in the literature, mainly for the lower density C-S-H. The amount of porosity (categorised as gel porosity) in the C-S-H has significant influence on its stiffness. A range between 13 GPa and 26 GPa, in accordance with Table 4, was adopted for Young's modulus of the outer C-S-H, to evaluate its influence on the effective Young's modulus of the REV. The obtained results from these analyses are plotted in Figure 16a. The influence of C-S-H stiffness at very early ages is not significant since the hydration degree is low and not much C-S-H product is formed yet. However, when the minimum value of 13 GPa was adopted for the outer C-S-H, the results from the FEM model overestimated the test results at very early ages. By increasing the degree of hydration, the higher stiffness for the outer C-S-H results in higher values for the effective elastic modulus of the REV.

To better show the influence of the C-S-H stiffness, particularly at very early ages, a single value was assumed for Young's modulus of C-S-H volumes in the REV. Then, a back-analysis was undertaken to fit the effective elastic modulus obtained from the model to the corresponding experimental result by varying Young's modulus of the C-S-H. The results of this back-analysis are plotted in Figure 16b. Additionally, the given value of the back-fitted Young's modulus of C-S-H is plotted as a secondary vertical axis in this figure. As shown, by decreasing Young's modulus of C-S-H at very early ages,

the effective Young's modulus from the model captures the experimental value. This can be an evidence that, at very early ages, only low dense C-S-H starts to form in the microstructure, which agrees with similar conclusions stated by other authors [38,39].

It should be noted that the volume ratio between the inner and outer C-S-H products is not constant during hydration, and it also has a dependency on the  $w/c$  ratio [39]. However, this influence is not controlled in the HYMOSTRUC3D hydration model, as almost the same volume ratio between the inner and outer C-S-H is assumed to form for any  $w/c$  ratio.

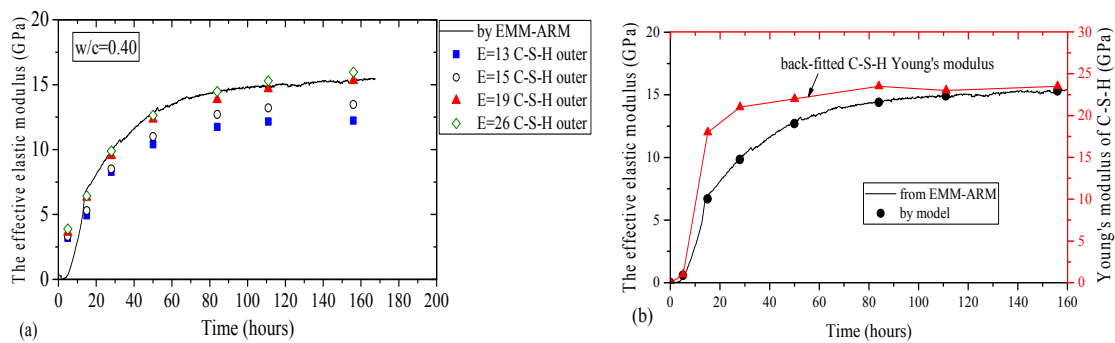


**Figure 16.** Effective Young's modulus of the cement paste in REV: (a) influence of the outer C-S-H Young's modulus; (b) influence of the average Young's modulus of C-S-H when it is assumed as a single-phase product with no division to inner and outer.

## 7. Summary and Conclusions

The present study investigated the evolution of the elastic properties of cement pastes, by performing a continuum micromechanics approach. The cement paste microstructure was simulated using the HYMOSTRUC3D hydration model on a cubic Representative Elementary Volume (REV) with periodic boundary conditions. The obtained REV microstructure was then discretised by using equal small cubic voxels, each one representing a single material phase. A lattice model built from truncated octahedrons was used to predict the elastic properties of the REV microstructure. A specific calibration of the bonds with lattice beams of circular cross-section was used to illustrate the ability of an improved lattice model to represent elastic properties accurately, particularly the Poisson's ratio. The strength of the lattice model to predict the elastic properties of a cement paste was first evaluated using the FEM modelling approach as a reference for comparison. The FEM model was constructed by converting cubic voxels to classical 8-noded solid hexahedral FEs. The elastic results from the two approaches matched reasonably well. Deviations of the lattice model predictions were further reduced when the elastic properties of lattice beam interfaces were based on the classical Hashin–Shtrikman bounds theory, rather than on the serial/parallel theory.

The effective Young's modulus of cement pastes predicted by the lattice and FEM models were then compared with the experimental measurements assessed during hydration by the EMM-ARM testing technique. Both numerical models showed good predictive performances for cement pastes with  $w/c$  ratios of 0.32 and 0.40. However, an underestimation of the effective elastic modulus was obtained for  $w/c = 0.48$  using both numerical models.

Based on a parametric study carried in the present study, the following conclusions can also be drawn:

- While the volume of cement was kept constant in the cement hydration modelling, a variation of the Particle Size Distribution (PSD) of cement grains resulted in different morphologies in the cement paste microstructure. When the number of particle increases (adopting a finer PSD curve), finer pore networks are formed, leading to a higher number of solid phase contacts in the microstructure. The higher number of solid connections increases the effective Young's modulus of the cement paste. The phenomenon was opposite when a coarser PSD curve was adopted.

Therefore, the pore network morphology has a strong influence on the numerical prediction of the effective elastic modulus of the cement paste.

- (ii). The voxel size, directly related to the microstructure discretisation, plays an important role when using numerical models for predicting the elastic modulus of cement pastes. To reduce the artificial solid connections in digitalised microstructures, the size of voxel shall be adequately small. Decreasing the voxel size to about 70% of the minimum size of cement grains seems to be a promising strategy to improve the accuracy of the numerical predictions.
- (iii). At very early ages, by decreasing Young's modulus of C-S-H the numerical models capture the experimental value of the effective Young's modulus of the cement paste. At these early ages, only low dense C-S-H starts to form in the microstructure, and consequently, a division of the C-S-H product into inner and outer phases leads to an overestimation of the effective Young's modulus of the cement paste.

**Acknowledgments:** This work was supported by projects POCI-01-0145-FEDER-007457 (CONSTRUCT—Institute of R&D in Structures and Construction) and POCI-01-0145-FEDER-007633 (ISISE—Institute for Sustainability and Innovation in Structural Engineering), funded by FEDER through COMPETE2020—Programa Operacional Competitividade e Internacionalização and by national funds through FCT—Fundação para a Ciência e a Tecnologia. FCT and FEDER (COMPETE2020), who are acknowledged for the funding of the research project PTDC/ECM-EST/1056/2014 (POCI-01-0145-FEDER-016841). The first author is also thankful for the grant with reference number SFRH/BPD/114754/2016 funded by FCT.

**Author Contributions:** R.F. and M.A. designed and directed the research project. H.M. developed and implemented the simulation models (FEM and lattice models), and prepared the manuscript. R. F. supervised the work, supported to drafting of the paper, and contributed to analyse the results. R.F., M.A. and H.M. discussed the results and implications and commented on the manuscript at all stages. G.Y. provided the hydration model (HYMOSTRUC3D) and gave technical support and conceptual advice. E.S. gave technical support and conceptual advice, mostly in case of lattice model. J.G. and M.A. contributed with EMM-ARM results and background information. M.A. supervised the work, and supported to drafting of the paper (highest contribution in Section 5).

**Conflicts of Interest:** The authors declare no conflicts of interest.

## References

1. Zaoui, A. Continuum micromechanics: Survey. *J. Eng. Mech.* **2002**, *128*, 808–816. [[CrossRef](#)]
2. Suquet, P. *Continuum Micromechanics*; Springer: Berlin/Heidelberg, Germany, 2014; Volume 377.
3. Montero-Chacón, F.; Marín-Montín, J.; Medina, F. Mesomechanical characterization of porosity in cementitious composites by means of a voxel-based finite element model. *Comput. Mater. Sci.* **2014**, *90*, 157–170. [[CrossRef](#)]
4. Jawed, I.; Skalny, J.; Young, J.F. Hydration of Portland cement. In *Structure and Performance of Cements*; CRC Press: Boca Raton, FL, USA, 1983; pp. 284–285.
5. Xiao, L.; Li, Z. New understanding of cement hydration mechanism through electrical resistivity measurement and microstructure investigations. *J. Mater. Civ. Eng.* **2009**, *21*, 368–373. [[CrossRef](#)]
6. Bullard, J.W.; Jennings, H.M.; Livingston, R.A.; Nonat, A.; Scherer, G.W.; Schweitzer, J.S.; Scrivener, K.L.; Thomas, J.J. Mechanisms of cement hydration. *Cem. Concr. Res.* **2011**, *41*, 1208–1223. [[CrossRef](#)]
7. Jennings, H.M.; Johnson, S.K. Simulation of microstructure development during the hydration of a cement compound. *J. Am. Ceram. Soc.* **1986**, *69*, 790–795. [[CrossRef](#)]
8. Bentz, D.P. *A Three-Dimensional Cement Hydration and Microstructure Program: I. Hydration Rate, Heat of Hydration, and Chemical Shrinkage*; Building and Fire Research Laboratory, National Institute of Technology: Gaithersburg, MD, USA, 1995.
9. Van Breugel, K. Numerical Simulation of Hydration and Microstructural Development in Hardening Cement-Based Materials. (I) Theory. *Cem. Concr. Res.* **1995**, *25*, 319–331. [[CrossRef](#)]
10. Ye, G. Experimental Study and Numerical Simulation of the Development of the Microstructure and Permeability of Cementitious Materials. Ph.D. Thesis, TU Delft, Delft University of Technology, Delft, The Netherlands, 2003.
11. Bishnoi, S.; Scrivener, K.L.  $\mu$ ic: A new platform for modelling the hydration of cements. *Cem. Concr. Res.* **2009**, *39*, 266–274. [[CrossRef](#)]

12. Mazaheripour, H.; Faria, R.; Ye, G.; Schlangen, E.; Granja, J.; Azenha, M. Microstructure-based modelling prediction of elasticity in hydrating cement paste. In Proceedings of the 2nd International RILEM/COST Conference on Early Age Cracking and Serviceability in Cement-Based Materials and Structures—EAC2 2017, ULB-VUB, Brussels, Belgium, 12–14 September 2017.
13. Schlangen, E.; Qian, Z. 3D modeling of fracture in cement-based materials. *J. Multiscale Model.* **2009**, *1*, 245–261. [[CrossRef](#)]
14. Qian, Z.; Ye, G.; Schlangen, E.; van Breugel, K. 3D lattice fracture model: Application to cement paste at microscale. *Key Eng. Mater.* **2011**, *452–453*, 65–68. [[CrossRef](#)]
15. Azenha, M.; Magalhães, F.; Faria, R.; Cunha, Á. Measurement of concrete E-modulus evolution since casting: A novel method based on ambient vibration. *Cem. Concr. Res.* **2010**, *40*, 1096–1105. [[CrossRef](#)]
16. Granja, J. Continuous Characterization of Stiffness of Cement-Based Materials: Experimental Analysis and Micro-Mechanics Modelling. Ph.D. Thesis, Civil Engineering Department, University of Minho, Braga, Portugal, 2016.
17. Muller, A.C.A.; Scrivener, K.L.; Gajewicz, A.M.; McDonald, P.J. Densification of C-S-H Measured by 1H NMR Relaxometry. *J. Phys. Chem. C* **2013**, *117*, 403–412. [[CrossRef](#)]
18. Velez, K.; Maximilien, S.; Damidot, D.; Fantozzi, G.; Sorrentino, F. Determination by nanoindentation of elastic modulus and hardness of pure constituents of Portland cement clinker. *Cem. Concr. Res.* **2001**, *31*, 555–561. [[CrossRef](#)]
19. Manzano, H.; Dolado, J.S.; Ayuela, A. Elastic properties of the main species present in Portland cement pastes. *Acta Mater.* **2009**, *57*, 1666–1674. [[CrossRef](#)]
20. Van Breugel, K. Numerical simulation of hydration and microstructural development in hardening cement-based materials:(II) applications. *Cem. Concr. Res.* **1995**, *25*, 522–530. [[CrossRef](#)]
21. Chang, C.S.; Wang, T.K.; Sluys, L.J.; van Mier, J.G.M. Fracture modeling using a micro-structural mechanics approach—I. Theory and formulation. *Eng. Fract. Mech.* **2002**, *69*, 1941–1958. [[CrossRef](#)]
22. Schlangen, E. Crack development in concrete, part 2: Modelling of fracture process. *Key Eng. Mater.* **2008**, *385–387*, 73–76. [[CrossRef](#)]
23. Wang, L.; Ueda, T. Mesoscale modelling of the chloride diffusion in cracks and cracked concrete. *J. Adv. Concr. Technol.* **2011**, *9*, 241–249. [[CrossRef](#)]
24. Šavija, B.; Pacheco, J.; Schlangen, E. Lattice modeling of chloride diffusion in sound and cracked concrete. *Cem. Concr. Comp.* **2013**, *42*, 30–40. [[CrossRef](#)]
25. Luković, M.; Šavija, B.; Schlangen, E.; Ye, G.; van Breugel, K. A 3D lattice modelling study of drying shrinkage damage in concrete repair systems. *Materials* **2016**, *9*, 575. [[CrossRef](#)] [[PubMed](#)]
26. Cusatis, G.; Bažant, Z.P.; Cedolin, L. Confinement-shear lattice CSL model for fracture propagation in concrete. *Comput. Methods Appl. Mech. Eng.* **2006**, *195*, 7154–7171. [[CrossRef](#)]
27. Jivkov, A.P.; Yates, J.R. Elastic behaviour of a regular lattice for meso-scale modelling of solids. *Int. J. Solids Struct.* **2012**, *49*, 3089–3099. [[CrossRef](#)]
28. *Element Library, in DIANA-10.1 User's Manual*; Manie, J. (Ed.) DIANA FEA: Delft, The Netherlands, 2017.
29. Timoshenko, S.; Goodier, J.N. *Theory of Elasticity*; NTNU: New York, NY, USA, 1951.
30. Karihaloo, B.L.; Shao, P.F.; Xiao, Q.Z. Lattice modelling of the failure of particle composites. *Eng. Fract. Mech.* **2003**, *70*, 2385–2406. [[CrossRef](#)]
31. Hashin, Z.; Shtrikman, S. A variational approach to the theory of the elastic behaviour of multiphase materials. *J. Mech. Phys. Solids* **1963**, *11*, 127–140. [[CrossRef](#)]
32. Sekkal, W.; Zaoui, A.; Benzerzour, M.; Abriak, N. Role of porosity on the stiffness and stability of (001) surface of the nanogranular C-S-H gel. *Cem. Concr. Res.* **2016**, *87*, 45–52. [[CrossRef](#)]
33. Boumiz, A.; Vernet, C.; Tenoudji, F.C. Mechanical properties of cement pastes and mortars at early ages: Evolution with time and degree of hydration. *Adv. Cem. Based Mater.* **1996**, *3*, 94–106. [[CrossRef](#)]
34. Ye, G.; van Breugel, K.; Fraaij, A.L.A. Three-dimensional microstructure analysis of numerically simulated cementitious materials. *Cem. Concr. Res.* **2003**, *33*, 215–222. [[CrossRef](#)]
35. Torrenti, J.-M.; Benboudjema, F. Mechanical threshold of cementitious materials at early age. *Mater. Struct.* **2005**, *38*, 299–304. [[CrossRef](#)]
36. Sun, Z.; Ye, G.; Shah, S.P. Microstructure and early-age properties of Portland cement paste—effects of connectivity of solid phases. *ACI Mater. J.* **2005**, *102*, 122–129.

37. Gao, P.; Ye, G.; Wei, J.; Yu, Q. Multi-scale simulation of capillary pores and gel pores in Portland cement paste. In Proceedings of the 14th International Congress on the Chemistry of Cement (ICCC 2015), Beijing, China, 13–16 October 2015.
38. Muller, A.C.A.; Scrivener, K.L.; Gajewicz, A.M.; McDonald, P.J. Use of bench-top NMR to measure the density, composition and desorption isotherm of C-S-H in cement paste. *Micropor. Mesopor. Mater.* **2013**, *178*, 99–103. [[CrossRef](#)]
39. Smilauer, V.; Bittnar, Z. Microstructure-based micromechanical prediction of elastic properties in hydrating cement paste. *Cem. Concr. Res.* **2006**, *36*, 1708–1718. [[CrossRef](#)]



© 2018 by the authors. Licensee MDPI, Basel, Switzerland. This article is an open access article distributed under the terms and conditions of the Creative Commons Attribution (CC BY) license (<http://creativecommons.org/licenses/by/4.0/>).